MNRAS **000**, 1–16 (2020) Preprint 13 April 2020 Compiled using MNRAS LATEX style file v3.0

Progenitor, Precursor and Evolution of the Dusty Remnant of the Stellar Merger M31-LRN-2015

N. Blagorodnova,[1] ⋆ V. Karambelkar,[2] S. M. Adams,[2] M. M. Kasliwal,[2] C. S. Kochanek,[3,4] S. Dong,[5] H. Campbell,[6] S. Hodgkin,[7] J. E. Jencson,[8] J. Johansson,[9] S. Kozłowski,[10] R. R. Laher,[11] F. Masci,[11] P. Nugent,[12] U. Rebbapragada [13]

[1] *Department of Astrophysics/IMAPP, Radboud University, Nijmegen, The Netherlands*
[2] *Cahill Center for Astrophysics, California Institute of Technology, Pasadena, CA 91125, USA*
[3] *Department of Astronomy, The Ohio State University, 140 W. 18th Ave., Columbus, OH 43210, USA*
[4] *Center for Cosmology and AstroParticle Physics (CCAPP), The Ohio State University, 191 W. Woodruff Ave., Columbus, OH 43210, USA*
[5] *Kavli Institute for Astronomy and Astrophysics, Peking University, Yi He Yuan Road 5, Hai Dan District, Beijing 100871, China*
[6] *Department of Physics, Faculty of Engineering and Physical Sciences, University of Surrey, Guildford, Surrey, GU2 7XH, UK*
[7] *Institute of Astronomy, University of Cambridge, Madingley Road, CB3 0HA, Cambridge, UK*
[8] *Steward Observatory, University of Arizona, 933 North Cherry Avenue, Tucson, AZ 85721-0065, USA*
[9] *Department of Physics and Astronomy, Division of Astronomy and Space Physics, Uppsala University, Box 516, SE-751 20 Uppsala, Sweden*
[10] *Astronomical Observatory, University of Warsaw, Al. Ujazdowskie 4, 00-478 Warszawa, Poland*
[11] *Infrared Processing and Analysis Center, California Institute of Technology, Pasadena, CA 91125, USA*
[12] *Lawrence Berkeley National Laboratory, Berkeley, CA 94720, USA*
[13] *Astrophysics Research Institute, Liverpool John Moores University, 146 Brownlow Hill, Liverpool, L3 5RF, UK*
[14] *Jet Propulsion Laboratory, California Institute of Technology, Pasadena, CA 91125, USA*

Last updated 13 April 2020; in original form 13 April 2020

ABSTRACT

M31-LRN-2015 is a likely stellar merger discovered in the Andromeda Galaxy in 2015. We present new optical to mid-infrared photometry and optical spectroscopy for this event. The transient brightened by ∼3 mag as compared to its progenitor. The complex precursor emission, which started ∼2 years before the nova event, may be explained by the binary undergoing Roche-lobe overflow. The dynamical mass loss from the outer Lagrange point L2 creates an optically thick outflow to power the observed brightening of the system. We find two possible periods of 16±0.3 and 28.1±1.4 days at different phases of the precursor lightcurve, possibly related to the geometry of the mass-loss from the binary. Although the progenitor spectral energy distribution shows no evidence of pre-existing warm dust in system, the remnant forms an optically thick dust shell 2–4 months after the outburst peak. The optical depth of the shell increases after 1.5 years, suggesting the existence of shocks that enhance the dust formation process. We propose that the merger remnant is likely an inflated giant obscured by a cooling shell of gas with mass $\sim 0.2\,M_\odot$ ejected at the onset of the common envelope phase.

Key words: binaries (including multiple): close – stars: evolution – (stars:) novae, cataclysmic variables – (ISM:) dust, extinction – ISM: jets and outflows

1 INTRODUCTION

Luminous red novae (LRNe) are an observational class of astrophysical transients with peak luminosities in between novae and supernovae ($-3 < M_V < -14$ mag), making them members of the "gap transients" population (Kasliwal 2012; Pastorello & Fraser 2019). LRNe represent astrophysical transients related to a total or partial ejection of the common envelope in a binary system. This class includes stellar mergers such as V838 Mon (Munari et al. 2002) and V1309 Sco (Mason et al. 2010). The observational class of Intermediate Luminosity Optical Transients (ILOT), although also

⋆ E-mail: n.blagorodnova@astro.ru.nl

located in the "gap", are transients like SN2008S, which are likely electron-capture supernovae (Botticella et al. 2009a; Prieto et al. 2009). After maximum light, stellar mergers quickly evolve towards colder (redder) temperatures, resembling K or M-type giant stars. Their spectra are characterized by hydrogen emission lines expanding at velocities $\lesssim 1000$ km s^{-1} and a forest of absorption lines for low ionization elements. At later stages, the progressively cooling photosphere shows the formation of molecules and new dust in the system, which quickly obscures the optical emission (Kamiński & Tylenda 2011; Kamiński et al. 2015).

Since the discovery of the first "red variable" 30 years ago (M31RV; Rich et al. 1989; Mould et al. 1990), mergers have been sporadically detected both within the Milky Way and nearby galaxies (< 30 Mpc). Although their fainter luminosities pose a challenge to their discovery, a few nearby well studied cases provided a great wealth of information about their origin as violently interacting binary systems. The best example to date is V1309 Sco (Mason et al. 2010). Archival data revealed it to be a contact eclipsing binary, whose period decreased exponentially for several years prior to the nova outburst (Tylenda et al. 2011).

Stellar mergers provide unique observational clues about the final catastrophic stages of binary interaction. The contact phase is initiated when one of the stars (typically the primary evolving off of the main-sequence) overfills its Roche lobe and starts unstable mass transfer towards its companion (see Izzard et al. 2012, for a detailed explanation). Alternatively, it can be initiated by the Darwin instability. The spin up of the primary component in an initially tidally-locked binary would extract angular momentum from the orbit, drive the orbital decay, and ultimately initiate Roche lobe overflow (Darwin 1879; Rasio 1995). This process may culminate with both stars orbiting inside a common envelope (Paczynski 1976). The less massive component quickly spirals inwards, transferring the angular momentum of the binary to the envelope. At the termination of this phase part (or all) of the envelope can be ejected, leaving a more compact binary, or a fully coalesced star.

Currently, there are important unresolved questions regarding each phase of a CE event (see Ivanova et al. 2013a, for a review). Initially, what conditions give rise to the event? What is the role of pre-outburst mass loss from the system (Pejcha 2014; Pejcha et al. 2016b,a)? Which systems undergoing Roche lobe overflow (RLOF) result in CE events via dynamically-unstable mass transfer? Is the transient powered primarily by recombination (Ivanova et al. 2013b) or by shock interaction between multiple shells of pre-existing material (Metzger & Pejcha 2017)? What is the role of dust driven winds in unbinding the loosely coupled envelope after its ejection (Glanz & Perets 2018)? Finally, understanding which common envelope events result in a complete merger and which result in a close binary binary is crucial for gravitational wave science.

Well studied stellar mergers are powerful probes of the phase of dynamical unset for common envelope evolution. Although the rate of these transients is high enough (Kochanek et al. 2014) to ensure several detections per year with ongoing surveys, such as the Zwicky Transient Facility (ZTF; Adams et al. 2018), few are likely to happen as close as M31. The event we discuss here, M31-LRN-2015, is probably the closest extragalactic example of this transient family for the next 20 years, and thus provides the best opportunity for studying the evolution of the remnant at late times.

M31-LRN-2015 was discovered in the Andromeda galaxy (M31) at $\alpha_{\rm J2000} = 00^{\rm h}42^{\rm m}07^{\rm s}.99$, $\delta_{\rm J2000} = +40^{\circ}55'01''.1$, (6.8′ W and −21.13′ S of its galaxy centre) on UTC 2015 January 13.63 by the MASTER survey (Shumkov et al. 2015a). Though the transient was initially classified as a classical nova peaking at $R \sim 15.1$ mag, it quickly evolved towards red colours and was re-classified as a LRN (based on its luminosity, slow decline, color evolution, and spectroscopic similarities to V838 Mon) by Kurtenkov et al. (2015c). Dong et al. (2015) identified a progenitor in archival Hubble Space Telescope (*HST*) imaging and noted that the progenitor had started brightening in later archival Canada France Hawaii Telescope (CFHT) photometry. Kurtenkov et al. (2015a), Williams et al. (2015), and Lipunov et al. (2017) presented optical and near infrared (NIR) light curves and optical spectra of the outburst spanning from ∼10 days pre-maximum to ∼60 days post-maximum.

Further analysis by MacLeod et al. (2017) used the archival photometry from Dong et al. (2015) and Williams et al. (2015) to estimate the evolutionary stage of the progenitor star for single stellar models. The best agreement was reached for a $3-5.5\,{\rm M}_{\odot}$ sub-giant star with a radius $30-40\,{\rm R}_{\odot}$ that was evolving off the main sequence. In their model, the optical transient lasted less than 10 orbits of the original binary, and the light curve was best explained by $\sim 10^{-2}\,{\rm M}_{\odot}$ of fast ejecta driven by shocks at the onset of CE followed by an additional $\sim 0.3\,{\rm M}_{\odot}$ ejected at slower velocities as the secondary continued to spiral in through the envelope of the primary.

Similar results were obtained by Lipunov et al. (2017), using hydrodynamic simulations designed to reproduce the multi-colour lightcurve of the transient. The observed ∼50 day plateau was explained by a stellar merger with a progenitor mass of $3\,{\rm M}_{\odot}$ and a radius of $10\,{\rm R}_{\odot}$, which underwent a fast shock, heating the base of the envelope and accelerating the matter to photospheric velocities of $v \sim 900\,{\rm km\,s^{-1}}$. In this scenario, the system is already a tight binary with a degenerate dwarf primary, and the unstable mass transfer is initiated by the secondary companion.

Alternatively, Metzger & Pejcha (2017) suggested that the M31-LRN-2015 light curve could be explained as an interaction of a dynamically ejected shell with preexisting equatorial material. In this case, a more extended period of mass loss from the L2 point powers the observed emission.

In this paper we present new optical and infrared photometry, and optical spectroscopic data on M31-LRN-2015. We investigate the evolution of the progenitor up to 5.5 years before the outburst, which shows a more complex behaviour. We also provide the first analysis of the remnant, based on infrared photometry taken up to 5 years after the outburst. We present new observational data in Section 2. Our analysis of the object's spectroscopic and photometric evolution is in Section 3. We discuss the implications of our results in Section 4 and summarize our conclusions in Section 5.

Table 1. Archival (see references) and follow-up photometry for M31-LRN-2015. These values have not been corrected for extinction. This table is shown as a guidance on the format. The full table is available as part of the online material.

Phase	MJD	Telescope	Filter	Mag	ATel
-3810.7	53233	HST	I	22.02±0.01	7173
-3810.7	53233	HST	V	23.2±0.03	7173
-3443.7	53600	Spitzer	3.6	>17.99	
-3443.7	53600	Spitzer	4.5	>17.83	
-3443.7	53600	Spitzer	5.8	>17.03	
-3443.7	53600	Spitzer	8.0	>15.89	
...	...	...	...	...	...
1260.8	58304.5	Keck	K	>24.26	
1291.8	58335.5	Keck	J	>25.27	
1291.8	58335.5	Keck	H	>24.81	
1793.2	58836.9	Spitzer	3.6	>17.2	
1793.2	58836.9	Spitzer	4.5	15.73±0.02	

References: ATel 7173 Dong et al. (2015)

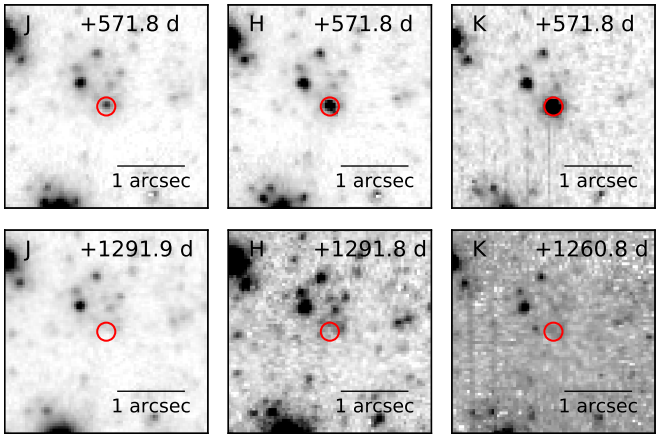

Figure 1. Late time follow-up of M31-LRN-2015 in J, H, Ks bands with Keck II/NIRC2-AO. The location of the target is indicated with a red circle. The remnant is clearly detected at 571.8 days (∼1.5 years), but at 1291.9 days the star has faded beyond the confusion limit. The cutouts have the standard orientation North:up, East:left.

2 OBSERVATIONS

2.1 Distance and reddening

Following Williams et al. (2015) and Lipunov et al. (2017) we adopt a distance of 0.762 Mpc, corresponding to a distance modulus of $(m-M) = 24.4$ mag (Freedman & Madore 1990).

There is some uncertainty in the reddening that should be adopted for M31-LRN-2015. Based on the foreground reddening of $E(B-V) = 0.062$ mag (Schlegel et al. 1998) and the total line-of-sight extinction at the position of M31-LRN-2015 of $E(B-V) = 0.18$ (Montalto et al. 2009), Williams et al. (2015) and Lipunov et al. (2017) assume M31-LRN-2015 was reddened by $E(B-V) = 0.12 \pm 0.06$ mag. Kurtenkov et al. (2015a) report a line of sight reddening of $E(B-V) = 0.42 \pm 0.03$ mag based on dust maps of M31 (Draine et al. 2014), and find $E(B-V) = 0.35 \pm 0.10$ mag from modeling spectra taken between UTC 2015 January 15 and 2015 February 24. In this paper we adopt a foreground extinction of $E(B-V) = 0.055$ based on the Schlafly et al. (2012) recalibration of the Schlegel et al. (1998) dust maps plus an average host extinction of $E(B-V) = 0.2$, which is a compromise between all previous studies. Therefore, the total extinction used in this study is $E(B-V) = 0.255$.

2.2 Photometry

We monitored the photometric and spectroscopic evolution of M31-LRN-2015 with a variety of ground-based facilities and with the *Spitzer Space Telescope* (SST; Werner et al. 2004; Gehrz et al. 2007). We also collected all the published data on this source from literature. A full log of archival and follow-up photometry is shown in Table 1.

The precursor and the nova photometry were retrieved from archival images from the Palomar Transient Facility (PTF; Law et al. 2009; Rau et al. 2009) and the Intermediate Palomar Transient Facility (iPTF; Kulkarni 2013). The images were obtained between MJDs 55569.0 and 57642.0 (5.3 prior to discovery to 1.6 years after) with the CFH12K camera (Rahmer et al. 2008; Law et al. 2010) on the Palomar 48-inch Telescope (P48). The PTF/iPTF data were processed with the PTF image subtraction pipeline `PTFIDE` (Masci et al. 2017). The CFHT/MegaPrime lightcurves with ∼6 and ∼26 min cadence were obtained from three full nights of monitoring of the M31 field for microlensing on 2014 October 24, 28 and 30 (PI: Subo Dong). The photometry was obtained using difference imaging analysis (Wozniak 2000) and calibrated using the Pan-STARRS release 1 (PS1) Survey -DR1 (Chambers et al. 2016).

Optical follow-up imaging was obtained with the Liverpool Telescope (Bersier et al. 2015) and with the Large Binocular Camera (LBC; Giallongo et al. 2008) on the Large Binocular Telescope (LBT; Hill et al. 2006).

Near-IR imaging was collected with the LBT NIR-Spectroscopic Utility with Camera and Integral-Field Unit for Extragalactic Research (LUCIFER; Seifert et al. 2003), with the CAmara INfrarroja (CAIN) on the Telescopio Carlos Sánchez and, at late times, with the NIRC2-AO camera on the 10 m Keck II telescope. The observations were made with J, H and K_s filters in the wide camera mode, having 40 mas pixel^{-1}. We used the laser guide star adaptative optics (LGS AO; Wizinowich et al. 2006) system to delivered diffraction limited images with an FWHM of approximately 2.5 pixels (equivalent to 0.1 arcsec), required to resolve the fading progenitor in a crowded M31 star field. Figure 1 shows the location of the outburst at 1.5 and 3.5 years after discovery.

Confusion complicates the interpretation of ground-based (seeing-limited) photometry of the progenitor and remnant. Archival images from Hubble Space Telescope (*HST*) obtained on UTC 2004 August 16 also reveal multiple sources within 1″ of the progenitor with fluxes comparable to that of the progenitor (Dong et al. 2015; Williams et al. 2015). Image subtraction via the PTFIDE pipeline for the PTF data and via ISIS for the LBT data enables accurate measurement of changes in flux, but not the total flux of the target. However, due to the faintness of the progenitor, we assume that the deviation from the total flux is negligi-

ble. The difference imaging precursor lightcurve is shown in Figure 2.

In our mid-IR follow-up (Figure 3), we utilize both new and archival mid-IR data in [3.6] and [4.5] from the Infrared Array Camera (IRAC; Fazio et al. 2004) on board *Spitzer Space Telescope*. Under programs 11181, 12063 PI: C. Kochanek), and 13053, 14089 (PI: M. Kasliwal), we obtained mid-IR imaging from UTC 2015 April 06 to UTC 2019 December 19). We also analyzed the archival images from UTC 2005 August 18/19 (program 3126; PI: P. Barmby)[1], and from 2015 taken under the program 11103 (PI: O. Jones). The *Spitzer* photometry was reduced using the difference imaging pipeline developed for the *Spitzer* InfraRed Intensive Transients Survey (SPIRITS) survey (Kasliwal et al. 2017).

2.3 Spectroscopy

We acquired optical follow-up spectra with the OSMOS spectrograph on the MDM Observatory 2.4 m Hiltner telescope on UTC 2015 March 10 (+47.4 days; Wagner et al. 2015) and with the Low Resolution Imaging Spectrograph (LRIS; Oke et al. 1995) on the 10 m Keck I telescope on UTC 2015 June 13 (+142.9 days). The OSMOS spectrum was reduced using a standard `IRAF` routines. The LRIS spectrum was reducing using an `IDL` based pipeline `lpipe` developed by D. Perley [2].

We also include early time (8 days pre-peak) spectroscopy from WHT/ACAM reported by Hodgkin et al. (2015) and the Liverpool Telescope SPRAT Spectroscopy published in Williams et al. (2015). The ACAM spectrum was reduced using the usual `IRAF` procedures, and scaled using the photometry in B and R bands of the nova reported for the same night by Kurtenkov et al. (2015a). The observation log for unpublished spectra is provided in Table 2 and the spectral sequence is displayed in Figure 4. Upon publication, these data will be made publicly available via the online repository `WiseREP` (Yaron & Gal-Yam 2012).

In order to correct the spectra for the systemic velocity of Andromeda, we adopt $v_{\rm sys} = 304.5 \pm 6.8\,{\rm km\,s^{-1}}$ (Chemin et al. 2009). In addition, we note that the relative position of the transient within the host galaxy (6.8′ W and 21.13′ S of M31 centre) is nearly aligned with the galaxy's semi-major axis. Assuming that the progenitor is a relatively young star (100 Myr for a 5 $M_\odot$) which still follows the galaxy rotation curve, we can estimate that the star may have an additional correction, related to its rotation within the galaxy $v_{rot} \sim$-200 km s^{-1}, which should be considered as an upper limit for any additional correction to the velocity.

[1] We do not use archival imaging from this program taken 2005-01-20/21 because a solar proton event flooded the detector with cosmic rays.
[2] `http://www.astro.caltech.edu/~dperley/programs/lpipe.html`

3 ANALYSIS

3.1 Spectroscopic Evolution

Our earliest spectrum was taken 8 days before optical peak. The fit for an extinction-corrected continuum shows a ∼5000 K black body emission along with narrow absorption lines for low-ionization elements such as Na I, Fe II, Sc II and Ba II. We also detect the Ca II triplet in absorption with a velocity of $-130\,{\rm km\,s^{-1}}$. Note the lack of emission lines for [Ca II], which are consistently observed in ILOTs (Botticella et al. 2009b; Bond et al. 2009) (see Figure 4). The peak of the Hα emission is located at 6558.8Å, indicating a redshift of $\sim$100 km s^{-1}. Although the line shows a multi-component profile, the FWHM of the emission indicates that the line is likely unresolved ($<$880 km s^{-1}). The Hβ line is detected in absorption, centered on 4855.7Å ($-50\,{\rm km\,s^{-1}}$) with a FWHM of $380\pm247\,{\rm km\,s^{-1}}$ (see Table 3 for fit results). The profile appears to be partly filled by an emission component, in agreement with the characteristics for the spectrum at −6 days reported by Fabrika et al. (2015) and Kurtenkov et al. (2015a).

The spectral sequences from Williams et al. (2015) and Kurtenkov et al. (2015a) show a quick progression (in ∼40 days) from an almost featureless spectrum, into a one dominated by strong absorption bands from recently formed molecules. The Hα emission line detected at early times seems to disappear between +11.3 and +37.3 days, which coincides with the duration of the lightcurve plateau (see marks in Figure 3). If the plateau is powered by recombination, this process must be occurring deeper in the ejecta, with any emission from hydrogen recombination being absorbed by the cooler outer shell.

Towards the end of the r-band plateau at +47.5 days, the spectrum resembles a K7III star, with strong Na I and Ba II absorption lines and TiO molecular absorption bands. The spectrum again shows the Hα line in emission, although its peak has shifted to $\sim -300\,{\rm km\,s^{-1}}$. This line likely comes from an expanding, cooling shell. Analogous to cool Mira stars (Kamiński et al. 2017), the emission is accompanied by absorption at $+200\,{\rm km\,s^{-1}}$, pointing to the existence of inflowing gas.

The final spectrum, taken on the decline of the plateau, shows an almost complete lack of continuum emission blueward of 8000Å, as the optical part of the spectrum has been totally absorbed by molecules, such as TiO , VO and Zr O, that are produced in O-rich atmospheres. The late time spectrum closely resembles the spectrum of the Mira star R Leo, classified at minimum as a M9e type (Gunn & Stryker 1983; Keenan et al. 1974). The Hα line is still present in emission with a similar blueshifted velocity and signs of an absorption profile at a similar velocity.

3.2 Spectroscopic comparison

In the context of stellar mergers, the spectroscopic evolution of M31-LRN-2015 appears closer to the events detected in our own Galaxy than the more luminous transients recently presented by Pastorello et al. (2019b). This last group, mainly consisting of mergers of more massive stars, usually displayed two peaks in their lightcurve: a first, fast, blue

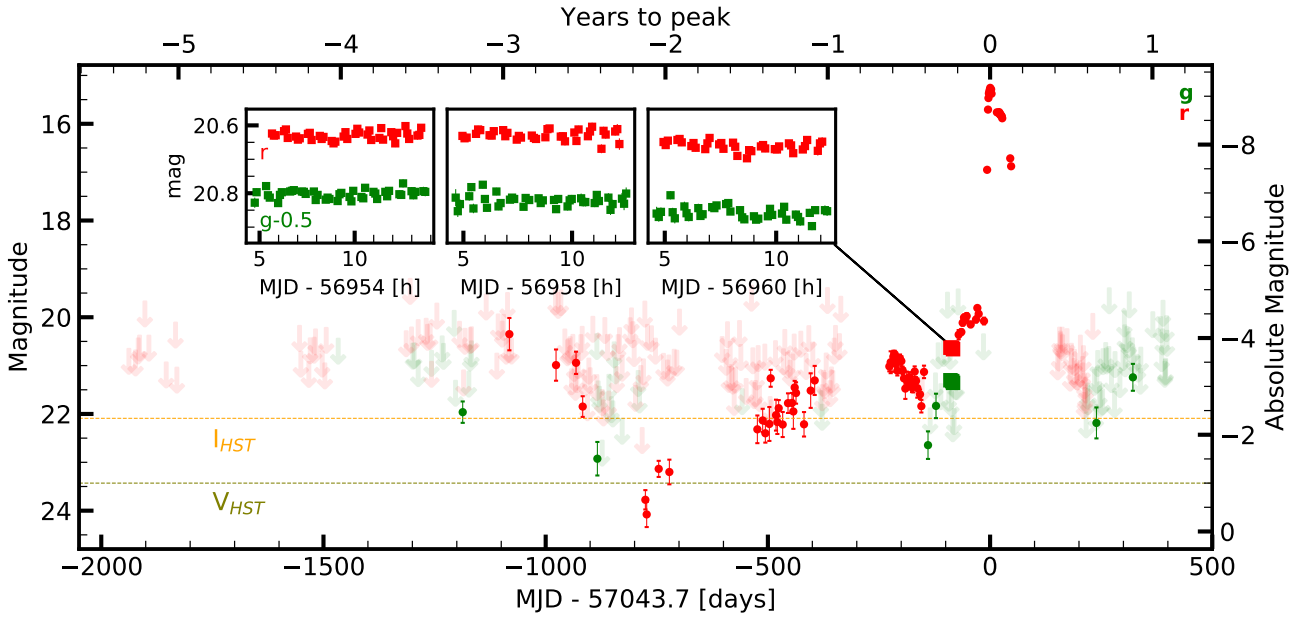

Figure 2. PTF/iPTF light curve of M31-LRN-2015 in Mould-R (red) and g bands (green). The lightcurve earlier than −20 days has been binned using a bin size of 3 days. At later dates, bins of 1 days were used. The HST progenitor limits at MJD 53233 (−10.4 years) reported by Dong et al. (2015); Williams et al. (2015) are shown as dashed horizontal lines. The green and red squares show the CFHT photometry. The measurement of the progenitor is reported in Dong et al. (2015). The insets show high cadence CFHT observations of the field on three full nights at −90, −86 and −64 days before peak.

Table 2. Log of spectroscopic observations of M31-LRN-2015.

Phase[a] (d)	MJD	UTC	Telescope +Instrument	Slit (arcsec)	Exposure (s)	Airmass	Resolution (km/s)	Hel. vel. (km/s)
−7.8	57035.88	2015-01-13T21:05:06	WHT+ACAM	1.5	1200	1.25	880	−25.6
+47.4	57091.11	2015-03-10T02:44:47	MDM + OSMOS	1.2	600	2.6	190	−16.2
+142.9	57186.58	2015-06-13T13:58:18	Keck I + LRIS	1.0	590	1.6	300	19.5

[a]The phase is relative to r-band peak date with MJD 57043.7.

Table 3. Fit parameters for the Hα and Hβ lines. The FWHM have been corrected for instrumental profile. The line fits were corrected for heliocentric velocity and for the systemic velocity of M31. The index "e" indicates the line emission component and the index "a" the absorption one.

Phase (day)	Ion	Velocity$_e$ (km s^{-1})	FWHM$_e$ (km s^{-1})	Velocity$_a$ (km s^{-1})	FWHM$_a$ (km s^{-1})
−8	Hβ	–	–	−48 ± 1	380 ± 247
−8	Hα	96±30	<880	–	–
+47.4	Hα	−309±1	115±30	−553 ± 14	136±22
+142.9	Hα	−304±1	300± 20	–	–

peak and a second, red peak, which sometimes is smoothed into a pleateau.

A comparison of the pre-peak spectra of M31-LRN-2015 with the extragalactic transient AT2017jfs (Pastorello et al. 2019a) (see Figure 5) shows an initial difference in the continuum temperature, which is also reflected in the emission lines seen during the first peak. AT2017jfs has an initial temperature corresponding to an ionized gas (⩾7000 K) and the spectrum shows signatures of interaction with an optically thick circumstellar medium (CSM), due to the strong electron scattering wings on the Balmer lines, Ca II and Fe II. On the other hand, the lower temperature of M31-LRN-2015 (∼5000 K) corresponds to mostly neutral gas and shows the same elements in absorption. The Hα and Hβ emission is likely related to recombination in an optically thin shell, surrounding the main outburst.

The evolution towards colder temperatures is similar to V838 Mon, where we see the appearance of TiO molecular absorption features. The Hα line, which disappeared between 21 and 37 days, starts to become detectable again at 47 days. We see very different signatures for spectra of ILOTs taken at a similar phase. For example, M51 OT2019-1 (Jencson et al. 2019a) shows a much hotter continuum, and broadened Balmer emission lines due to electron scattering. These transients also show the Ca II $\lambda\lambda$ 3933, 3968

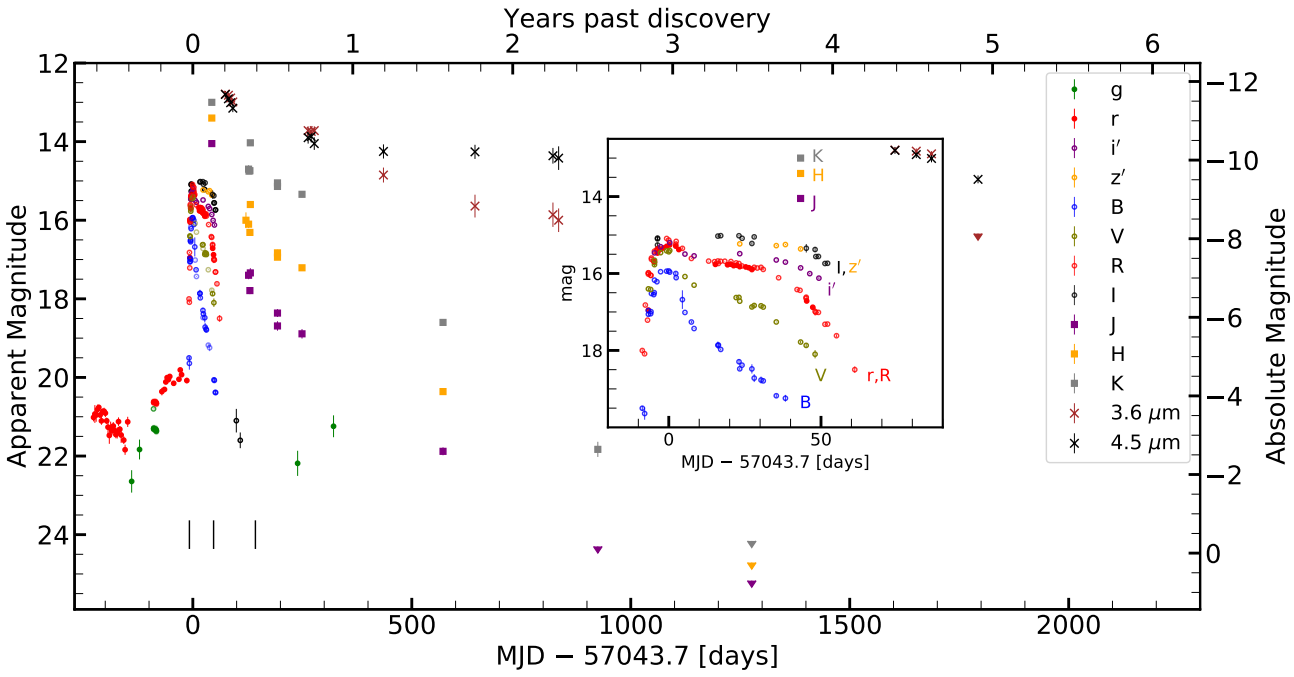

Figure 3. Lightcurve showing PTF/iPTF photometry, along with our NIR and MIR data. For better clarity, we added the measurements published by Williams et al. (2015) and Kurtenkov et al. (2015a) and ATels (Ovcharov et al. 2015; Kurtenkov et al. 2015b; Shumkov et al. 2015b; Srivastava et al. 2015; Pessev et al. 2015a; Adams et al. 2015a,b; Steele et al. 2015; Pessev et al. 2015b; Harmanen et al. 2015; Pessev et al. 2015c,d; Geier & Pessev 2015). Downward triangles show upper limits. The inset shows the lightcurve around peak. The vertical marks under the lightcurve show the times when our follow-up spectra were obtained. The complete photometry is given in Table 1.

doublet in absorption, where de-excitation leads to emission in the Ca NIR triplet, followed by a final forbidden transition of [Ca II] $\lambda\lambda$ 7291, 7323. This emission is not detected in LRNe.

The late time spectrum of M31-LRN-2015 is analogous to other Galactic (V1309 Sco; Kamiński et al. 2015) and extragalactic (M101-OT2015; Blagorodnova et al. 2017) stellar mergers. The cold stellar photosphere shows almost no flux at wavelengths shorter than 7000Å, and the spectrum is dominated by molecular absorption features. Some low-ionization elements are detected as narrow emission lines, likely generated in an optically thin shell irradiated by unobscured emission from the central object. The increased optical depth due to formation of dust can also explain the blueshift commonly observed in the the Hα profiles.

3.3 Constraints on progenitor dust

Based on the archival analysis of the SDSS and CFHT imaging presented in Dong et al. (2015), we can argue that the progenitor star for M31-LRN-2015 did have a relatively constant optical luminosity between 2002 and 2009. The photometry derived for this period agrees with the HST magnitudes $V = 23.2 \pm 0.03$ and $I = 22.02 \pm 0.01$ in 2004, about 10.4 years before the outburst peak (Dong et al. 2015; Williams et al. 2015). The constant luminosity of the progenitor allows us to combine the optical data with *Spitzer* upper limits obtained 9.4 years before the outburst, and to place constraints on the pre-existing dust in the system.

Our simple progenitor model assumes optically thin dust of uniform grain size $a = 0.1\mu$m, which radiates at a single equilibrium temperature T_d. Given the abundance of oxygen-rich molecules in the ejecta of LRNe, we assume silicate dust for our analysis. The assumption of a different dust composition does not significantly alter our results.

The specific luminosity for a dust grain of radius a and temperature T_d radiating at wavelength λ is given by

$$l_\nu(\lambda) = 4\pi a^2 B_\nu(\lambda, T_d) Q_{ext}(\lambda), \quad (1)$$

where $B_\nu(\lambda, T_d)$ is the Plank function, and $Q_{ext} = Q_{abs} + Q_{sca}$ is the dust efficiency factor for extinction (absorption plus scattering). For silicate dust we use the tabulated values of Laor & Draine (1993)[3]. Introducing the dust opacity, $\kappa(\lambda, a) = 3Q_{ext}(\lambda)/4\rho_d a$, where ρ_d is the dust bulk density ($\rho_d = 2.2\,\mathrm{g\,cm^{-3}}$ for graphitic dust and 3.5 $\mathrm{g\,cm^{-3}}$ for silicate), we can rewrite the equation as

$$l_\nu(\lambda) = 4M_d \pi B_\nu(\lambda, T_d)\kappa(\lambda, a) \quad (2)$$

[3] Available from https://www.astro.princeton.edu/~draine/dust/dust.diel.html

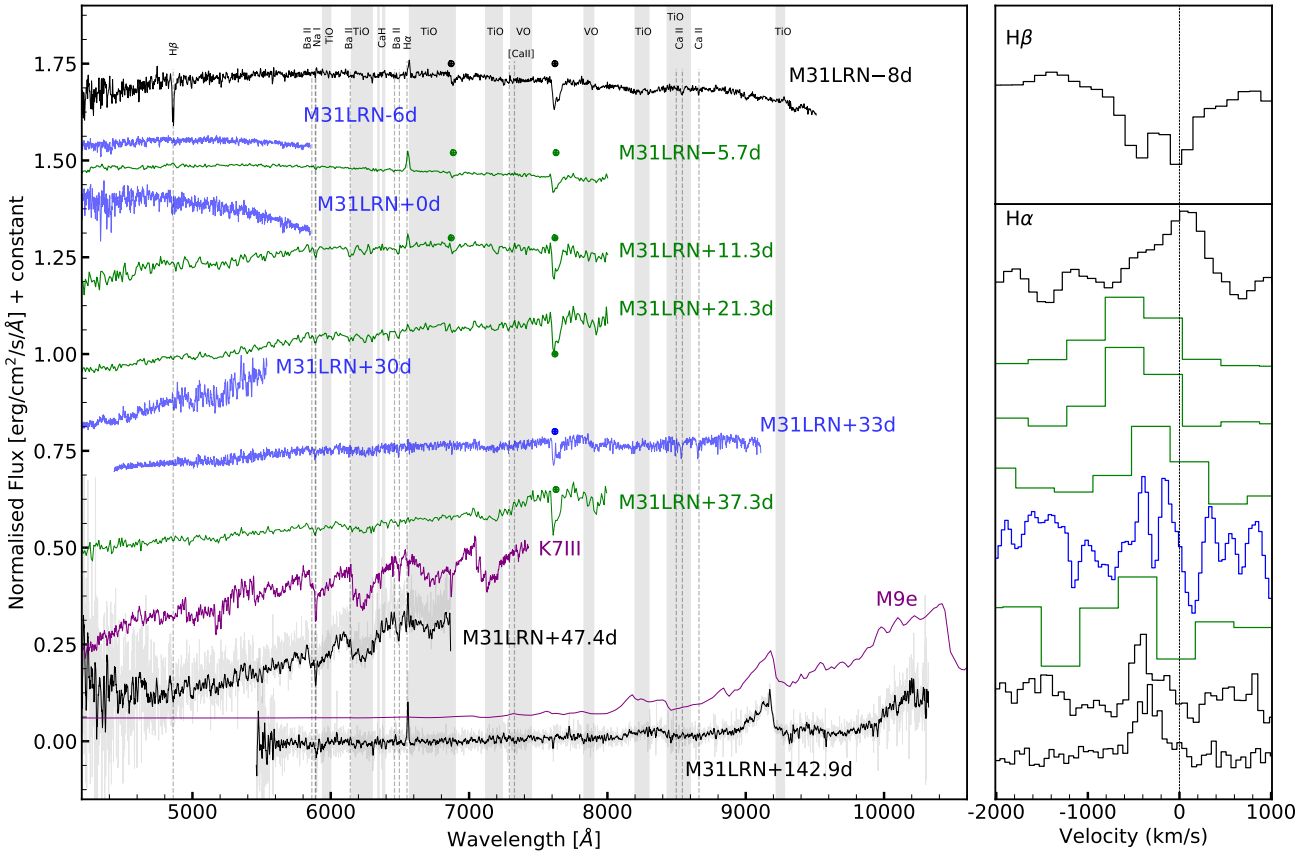

Figure 4. Left: Optical spectral sequence for M31-LRN-2015. The object spectra are colour coded by source. Our follow-up spectra are shown in black. A K7III spectrum (Jacoby et al. 1984) and M9e (Gunn & Stryker 1983) stellar spectra are shown in purple for comparison. As part of the sequence, we also included in green the LT spectra from Williams et al. (2015) and in blue the spectra from Kurtenkov et al. (2015a). The main element lines have been identified with dashed vertical lines. Molecular absorption bands are shown with gray rectangles. Right: Continuum subtracted and peak normalized profiles for the Hβ and Hα lines.

where M_d is the dust mass. The flux density for an observer at distance d is

$$F_\nu(\lambda) = \frac{M_d B_\nu(\lambda, T_d)\kappa(\lambda, a)}{d^2} \quad (3)$$

For our analysis of the progenitor SED, we initially fit the optical HST magnitudes with a single black body to estimate its contribution to the mid-infrared flux. The best fit given our extinction is $T = 4336^{+41}_{-43}$ K, $R = 46^{+2}_{-1}$ R$_\odot$ and bolometric luminosity of $L = 681^{+64}_{-53}$ L$_\odot$. Next, for each dust temperature $50 \leqslant T_d \leqslant 1500$ K, we derived the maximum dust mass M_d that is still consistent with a non-detection.

Our results, depicted in Figure 6, show that although the temperature has a strong influence on the dust mass, we still can place meaningful constraints for warmer dust. For example, for the hottest temperatures of $T_d = 1000 - 1500$ we find that $M_d < (10^{-9.2} - 10^{-9.7})$ M$_\odot$ and for $T_d = 500$ K $M_d < 10^{-8.0}$ M$_\odot$. For temperatures of 300 K and 100 K the peak of the emission shifts further into the far infrared, increasing the limits to $10^{-6.9}$ M$_\odot$ and $10^{-1.7}$ M$_\odot$. Due to the lack of far infrared measurements, our limits for colder dust are not that constraining, so we can not rule out the presence of a cold ($\sim$30 K) dust shell, such as the one detected for the remnant of V1309 Sco (Tylenda & Kamiński 2016).

3.4 Pre-outburst progenitor evolution

The extensive coverage of M31 by CFHT and the PTF/iPTF surveys since 2010 has provided us enough data to study the evolution of the progenitor up to five years before its outburst. Using the `PTFIDE` pipeline, we obtained hundreds of forced photometry measurements for observations taken between 2010 and the onset of the nova in January 2015, as shown in Figure 2. The Mould-R band luminosity remained mostly below our detection threshold up to 2 years before the outburst. After that, in what we call phase 1, it steadily increased in brightness by nearly two magnitudes between -2 and -1 years. During phase 2, at the start of the summer 2014 (-250 days) the progenitor was an additional magnitude brighter than in spring 2014, but faded by nearly a magnitude over the next three months. During phase 3, starting about 150 days prior to the January 2015 outburst, the Mould-R band flux reached its overall maximum of $\sim$20 mag and then remained relatively steady, with some minor fluctuations.

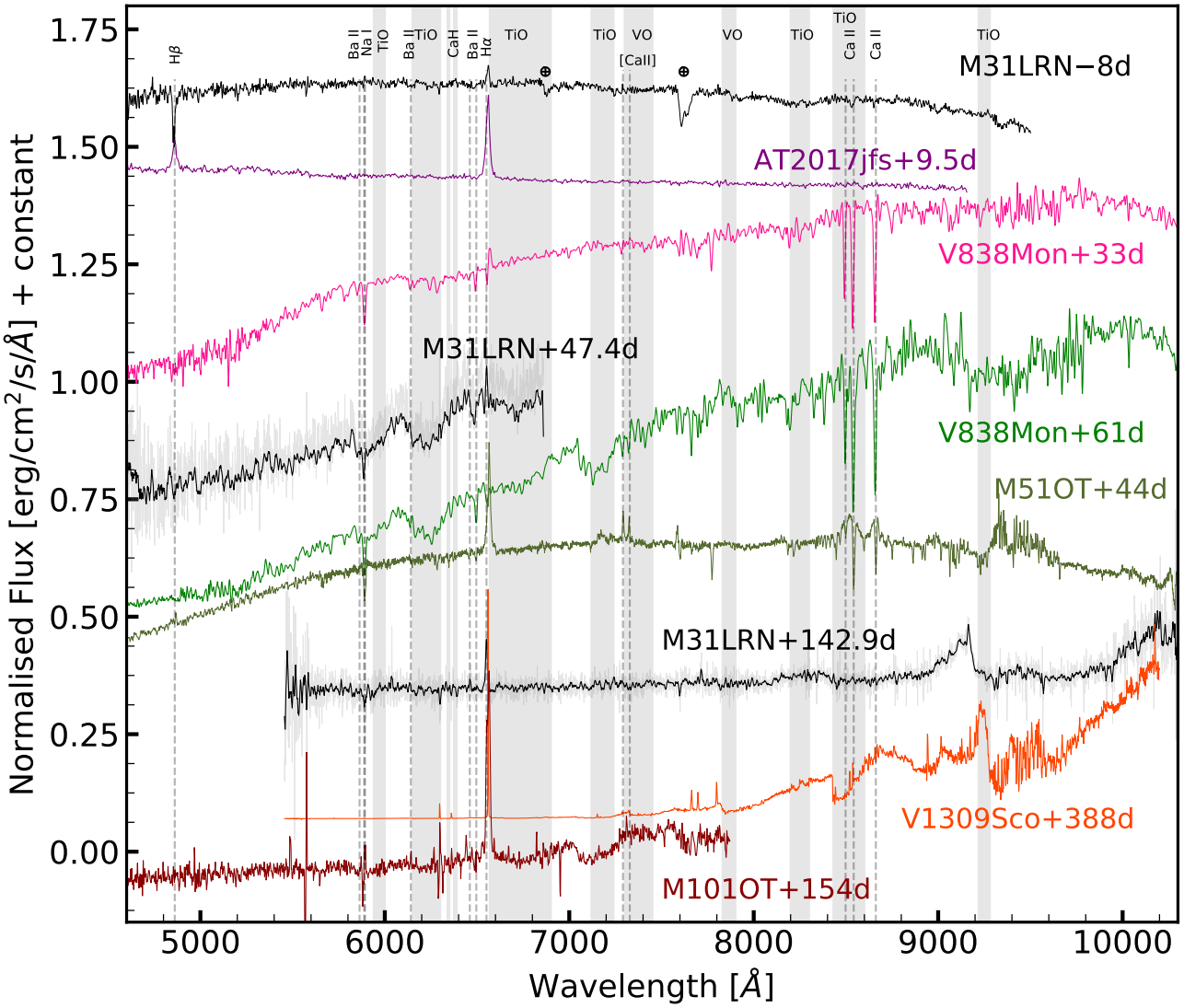

Figure 5. Spectral evolution of M31-LRN-2015 (shown in black) compared to other "gap" transients at similar epochs. The spectra of the massive stellar merger AT2017jfs (Pastorello et al. 2019a) during the first peak is shown in purple, the intermediate mass merger V838 Mon (Smith et al. 2016) in pink and green, the ILOT M51-OT2019 (Jencson et al. 2019a) is shown in olive, the low-mass merger V1309 Sco (Kamiński et al. 2015) in orange, and the massive merger M101-OT2015 (Blagorodnova et al. 2017) in brown.

CFHT data taken at about 3 months before eruption (Dong et al. 2015) agrees with iPTF observations (see insets in Figure 3). A single black body fit to the g and r-bands SED shows that the temperature of the emission was 6300^{+500}_{-500} K with a radius of 55^{+10}_{-10} $R_\odot$, which indicates that the precursor emission became hotter than the progenitor and its photospheric radius increased. The lack of extensive simultaneous multi-band photometry during the whole precursor period makes it difficult to determine whether the optical luminosity is linked to the apparent expansion and cooling of the photosphere, similar to the behaviour displayed by other stellar mergers such as V1309 Sco (Pejcha et al. 2017) or M101-2015OT (Blagorodnova et al. 2017), or to tidal heating, as argued by MacLeod et al. (2017). Like other stellar mergers, M31-LRN-2015 also shows a smooth, monotonic brightening lasting about two years. After this, the lightcurve also shows a dip, followed by a short precursor, similar to the one observed for V838 Mon (Munari et al.

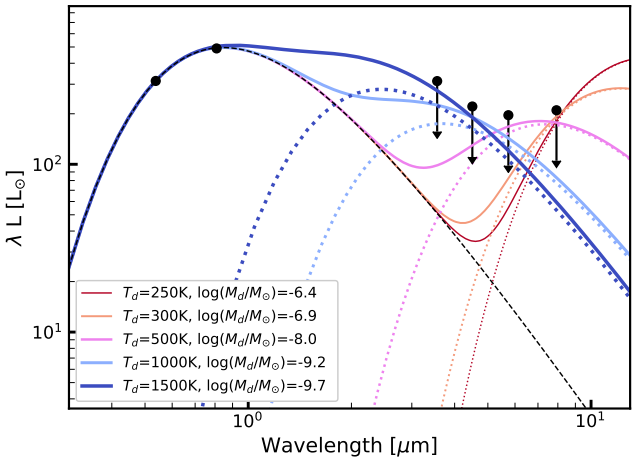

Figure 6. Limits for silicate ($a = 0.1\mu$m) dust emission component in the progenitor SED. The black points indicate the optical photometric measurements and the infrared upper limits. The black dashed line shows the black body fit to the progenitor photometry. The coloured dashed lines show the dust emission model at different temperatures T_d for a maximum dust mass M_d. Solid lines of the same colour indicate the total flux emitted by the star and the dust.

2002) or V1309 Sco. This behaviour is likely too complex to be caused by tidal heating. A possible explanation is the loss of mass from the system through the the L2 point during the RLOF, as proposed by Pejcha et al. (2017).

Mass loss progressively forms a decretion disk, draining angular momentum from the binary, which causes the orbit to shrink. This outflow can form an expanding photosphere around the binary. Pejcha et al. (2017) showed that the slow rise of V1309 Sco for thousands of orbits prior to merger could be explained by such dynamical mass loss. Assuming that the brightening in phase 1 of M31-LRN-2015 is due to an expanding optically thick outflow, we would expect the luminosity to scale as $L \propto (\dot{P}/P)^2$, where P is the period of the system. As the mass loss increases, the outflow is expected to completely engulf the binary, thereby causing the luminosity to decrease (phase 2). The observed emission now comes from shock interactions created by the L2 outflow. Depending on the binary mass ratio, further mass loss from the system can either form an expanding photosphere, or be marginally bound to the binary and interact with it. Either of these scenarios leads to a gradual increase in the luminosity (phase 3), as the orbit shrinks further until the binary finally merges, leading to the outburst.

Though the general trend of the M31-LRN-2015 light curve is similar to that of the V1309 Sco, there are a few differences. The most prominent difference is that the pre-outburst brightening of V1309 Sco smoothly transitioned into the outburst, with the photosphere expanding $\propto \dot{P}/P$, whereas for M31-LRN-2015 the pre-outburst brightening reached a constant value before the main outburst. In this regard, M31-LRN-2015 is more similar to V838 Mon. Before its first eruption, V838 Mon brightened by more than 3 mags and plateaued for around 25 days (Munari et al. 2002). Tylenda (2005) found that during this phase, the photospheric radius of V838 Mon remained almost the same. This could occur if the mass ejected during the brightening is marginally bound, and falls back to interact with the binary (Pejcha et al. 2016a). A necessary, but not sufficient condition for this to happen is the binary mass ratio q to be < 0.064 or > 0.78.

Close inspection of phases 2 and 3 shows that the residuals seem to be correlated once the general trend is removed, as the scatter in our measurements is larger than the error bars (the uncertainties for phase 1 are too large for a reliable analysis). Similar characteristics were observed for V1309 Sco (Pejcha et al. 2017), where the amplitude of the residuals oscillated by 0.3 mag. Deviations from the $(\dot{P}/P)^2$ rise were observed, but no period could be determined for the residuals. These residuals were interpreted as being due to the clumpiness and asymmetry of the mass lost from the binary. Motivated by the apparent correlation, we tested our lightcurve for periodicity in phase 2 (between MJD 56800−56895) and phase 3 (MJD 56960−57035). After removing a linear trend from our data, we used the Lomb-Scargle (Lomb 1976; Scargle 1982) algorithm, to produce a periodogram using different binnings and offsets of the bins. For phase 2, none of our best fits exceeded a power of 0.5, indicating a low significance for any period. However, the results consistently show one best period around 17 days (see Fig. 7). Averaging all the periods for binnings from 1 to 4 days (weighted by their power) allows us to derive a possible period of 16.8 ± 0.3 days. For phase 3, the power increases above 0.7. The average period for this phase is 28.1 ± 1.4 days, nearly double than for phase 2.

If the period detected in phase 2 is real, its variability can be used to infer the characteristics of the binary system. MacLeod et al. (2017) derived a mass of 3−5.5 $M_\odot$ and a radius of $\sim$35$R_\odot$ for the primary (depending on reddening). The period of a test mass at the surface of this binary is $13 - 6$ days depending on the mass. However, if the primary is undergoing RLOF, then the period for the binary for a mass ratio of $0.01 \leqslant q \leqslant 1$ is in the range of 390−39 days for a primary of 3.5 $M_\odot$ and 312−31 days for a more massive primary of 5.5 $M_\odot$.

Our first period of $\approx$ 17 days seems to be placed just in between the two cases, although an ellipsoidal variation would actually imply a period twice as large. Ideally, this variability should also be detected in earlier phases of the light curve, but the low SNR of the individual detections in phase 1 of our light curve makes this period difficult to analyse. The detection of a longer period in the late phase 3 is more consistent with a RLOF scenario for a binary with nearly equal mass ratio. However, detection of periodicity at this stage is nevertheless surprising, as the binary is expected to be completely engulfed at this point. An apparent increase in the period was observed in the early phases of the V1309 Sco light curve, when the phased light curve changed from a double hump profile to a single hump, effectively doubling the detected period from 0.7 to 1.4 days (Tylenda et al. 2011). This doubling of the period was attributed to the asymmetric nature of the L2 mass loss, in that the ejected mass trailed around the binary and partly obscured the system. Provided the period for M31-LRN-2015 has increased by nearly a factor of 2 from phase 2 to phase 3, it could possibly be a manifestation of the same phenomenon as in V1309 Sco. It is also likely that the binary is in fact com-

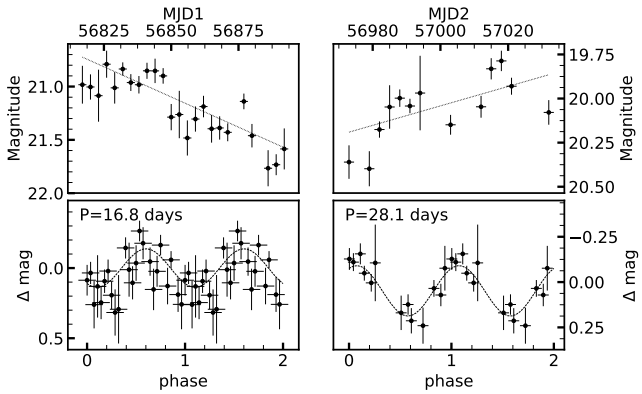

Figure 7. Left: 3-day binned R-band lightcurve for phase 2 (top) and the folded lightcurve using the best average period of 16.8 days (bottom). Right: 3-day binned lightcurve for phase 3 (top) and folded lightcurve with a period of 28.1 days (bottom). The error bars in the X-axis represent the width of the bin. All panels show the best linear polynomial fit used to remove the continuum, as well as the model lightcurve for the corresponding period.

pletely engulfed by the dust at this point, and the observed period is a result of interactions in the L2 mass outflow, as analyzed for the lightcurve of V1309 Sco (Pejcha 2014).

3.5 Post-Outburst Remnant Evolution

The late time photometric evolution of M31-LRN-2015 was monitored in the infrared by a combination of ground and space telescopes, as detailed in Section 2.2. In order to analyze the SEDs of the transient, we fixed the times and values for the NIR observations, and linearly interpolated the *Spitzer* and optical observations to those epochs. In total, we obtained the SED for seven post-peak epochs from at 43 days up to ∼3.5 years post peak.

Following the methods of Adams & Kochanek (2015) and (Adams et al. 2016, 2017), we modelled the SEDs with the dusty radiative transfer code DUSTY (Ivezic & Elitzur 1997; Ivezic et al. 1999; Elitzur & Ivezić 2001). In these models, DUSTY is embedded in an Markov Chain Monte Carlo (MCMC) wrapper to estimate the model parameters and their uncertainties. For the central source, we assume the stellar atmospheric models from Castelli & Kurucz (2004) for stars of solar composition but with various temperatures. We assume a prior on the temperature of the stellar remnant of $2500 \leqslant T_* \leqslant 20000$ K. The dust is treated as a shell with constant velocity v_{ej} and density profile $\rho \propto r^{-2}$. We fix the outer radius of the dust shell to be twice the inner dust radius. We examine optical depth values in the visual band within the range $0.16 \leqslant \tau_V \leqslant 1000$.

For our analysis, we tried with both silicate and graphitic grains from Draine & Lee (1984). For the dust grain sizes, we assume the standard MRN (Mathis et al. 1977) distribution function given by $n(a) \propto a^{-q}$, $a_{\rm min} < a < a_{\rm max}$ with q = 3.5, $a_{\rm min} = 0.005\mu$m and $a_{\rm max} = 0.25\mu$m. Finally, the reddening from the Milky Way and within the host galaxy was included as a fixed parameter with $E(B-V)$=0.255.

One limitation of our analysis is the assumption of spherical symmetry. Outflows from stellar mergers are likely equatorial, due to previous episodes of mass loss in the binary orbital plane (Metzger & Pejcha 2017). Therefore, the estimated dust optical depth could be an over or underestimation depending on the viewing angle.

The best fit models for both silicate and graphitic dust analysis are shown in Figure 8. The model parameters and their 1σ uncertainties are provided in Table 4, and depicted in Figure 9. Next we highlight the most important results of our analysis.

The DUSTY analysis of the progenitor SED obtained at −3795 days (10.4 years prior to the outburst) favours optically thin dust. Provided our analysis in Section 3.5, for a dust temperature of $T_d \sim 400$ K the total dust mass in the system was below $10^{-6}\,{\rm M}_\odot$.

Our earliest full optical to MIR SED is located towards the end of the r-band plateau at 43 days. At this stage, the transient is well-fit by a single component ≃3400 K blackbody and a radius of $1700\,{\rm R}_\odot$, which is consistent with the size of the ejecta if assuming that it expanded at a uniform velocity of $300\,{\rm km\,s^{-1}}$. When dust is included in the model, we obtain the same temperature for the central star. The value for the inner radius of the optically thin dust shell is located at ∼5000 $\rm R_\odot$, outside of the star's photosphere. The overall outburst luminosity is in agreement with the value derived by MacLeod et al. (2017) based on a blackbody model. Our spectrum taken at +47.4 days already shows signs for TiO absorption, in agreement with a cold stellar temperature. The outer colder shell, which has a dust temperature of ≃1750 K, would allow the dust condensation process to take place. If ejected around peak luminosity, the larger extent of this shell implies its velocity would be larger than the one of the photosphere, with $1350^{+350}_{-415}\,{\rm km\,s^{-1}}$. The most likely scenario is that this shell was already formed during the years or months preceding the eruption. For example, if the gas travelled from the system at escape velocity of $\sim 250\,{\rm km\,s^{-1}}$ (MacLeod et al. 2017), a shell of thin radius would have been ejected ∼160 days before the outburst peak, which coincides with the luminosity increase in the transient's lightcurve (phase 3).

By 127 days, the central source appears slightly hotter than during the plateau, with $T_* \simeq 4500$ K. However, the emission in the optical has almost faded below detection, as the dust shell has become optically thick ($\tau_V \simeq 19$) and has started to reprocess the radiation from the obscured star. The shell maintains a temperature of $T_d \sim 1700$ K, which is close to the threshold for the condensation of O-rich minerals (Lodders 2003).

A couple of months later, at 193 days and 249 days, we observe a continuous decrease in the bolometric luminosity of the source. Although the temperature of the star increases to $T_* \sim 7000$ K, the temperature of the dust shell remains relatively constant, as well as its optical depth.

A major change in the system is observed at 571 days (∼1.5 years post-outburst). At this time, the SED has clearly developed two distinct emission components. While the temperature of the central star has risen even further to $T_* \sim 10^4$ K, the temperature of the dust has cooled to ∼800 K. The shell also appears four times larger than before with $R_{\rm in} \sim 1.6 \times 10^4\,{\rm R}_\odot$.

After this phase, our last two epochs taken at 2.5 and

Table 4. Posterior parameter from DUSTY MCMC models of the remnant SED. The uncertainties give 1σ levels. L_* is the bolometric luminosity of the source, T_* is the intrinsic effective temperature of the input SED, $\tau_{V,\rm tot}$ is the optical depth of the shell in V-band, $R_{\rm in}$ is the inner radius of the dust shell, where the dust has temperature $T_{\rm d}$. $R_{\rm out}/R_{\rm in}$ is the thickness of the dust shell, $v_{\rm ej}$ is the velocity of the shell (assuming a constant expansion rate), χ^2 is the fit of the model and $M_{\rm ej}$ the ejecta mass computed using Eqn. 5. For the analysis, we adopted the local $E(B-V)$=0.2 in M31 in addition to $E(B-V) = 0.055$ for Galactic extinction.

Dust model	Date [UTC]	Phase [d]	log $(L_*/L_\odot)$	T_* [K]	$\tau_{V,\rm tot}$	log $(R_{\rm in}/{\rm cm})$	$T_{\rm d}$ [K]	log $(v_{\rm ej}/{\rm km\ s^{-1}})$	$\chi^2_{\rm min}$	$M_{\rm ej}$ [$M_\odot$]
silicate	2004-08-16	-3811	$2.78^{+0.09}_{-0.04}$	5850^{+900}_{-660}	$0.8^{+0.8}_{-0.5}$	$14.48^{+0.29}_{-0.29}$	440^{+220}_{-140}	$2.49^{+0.29}_{-0.29}$	$1.8^{+2.4}_{-1.2}$	$7.8^{+33.5}_{-6.5} \times 10^{-6}$
silicate	2015-03-06	43	$5.49^{+0.01}_{-0.01}$	3390^{+240}_{-130}	$0.7^{+0.8}_{-0.5}$	$14.54^{+0.16}_{-0.11}$	1760^{+170}_{-250}	$3.2^{+0.16}_{-0.11}$	$12.4^{+3.4}_{-2.3}$	$1.0^{+2.6}_{-0.8} \times 10^{-5}$
silicate	2015-05-29	127	$4.54^{+0.03}_{-0.02}$	4500^{+3210}_{-1470}	$19.0^{+3.8}_{-5.1}$	$14.4^{+0.15}_{-0.11}$	1740^{+160}_{-190}	$2.63^{+0.15}_{-0.11}$	$26.1^{+3.5}_{-1.7}$	$1.5^{+0.8}_{-0.5} \times 10^{-4}$
silicate	2015-08-03	193	$4.43^{+0.05}_{-0.03}$	6670^{+4360}_{-2560}	$20.2^{+3.6}_{-5.4}$	$14.47^{+0.19}_{-0.12}$	1680^{+180}_{-180}	$2.53^{+0.19}_{-0.12}$	$32.3^{+3.7}_{-1.9}$	$2.2^{+1.7}_{-0.8} \times 10^{-4}$
silicate	2015-09-28	249	$4.32^{+0.05}_{-0.03}$	7120^{+4490}_{-2970}	$22.3^{+4.0}_{-5.6}$	$14.43^{+0.2}_{-0.13}$	1680^{+180}_{-200}	$2.38^{+0.2}_{-0.13}$	$28.4^{+3.7}_{-2.0}$	$2.0^{+1.9}_{-0.7} \times 10^{-4}$
silicate	2016-08-15	571	$4.09^{+0.11}_{-0.11}$	10450^{+2280}_{-1700}	$27.3^{+3.9}_{-4.4}$	$15.07^{+0.13}_{-0.12}$	840^{+50}_{-50}	$2.68^{+0.13}_{-0.12}$	$3.7^{+3.4}_{-2.0}$	$4.7^{+3.7}_{-2.0} \times 10^{-3}$
silicate	2017-08-03	924	$3.84^{+0.08}_{-0.06}$	9780^{+6200}_{-5090}	$287.2^{+324.7}_{-113.2}$	$14.75^{+0.13}_{-0.08}$	1110^{+210}_{-190}	$2.15^{+0.13}_{-0.08}$	$3.1^{+2.1}_{-0.7}$	$1.3^{+0.9}_{-0.5} \times 10^{-2}$
silicate	2018-07-21	1276	$4.12^{+0.26}_{-0.19}$	9360^{+6340}_{-4690}	$415.2^{+280.7}_{-157.8}$	$15.3^{+0.26}_{-0.22}$	700^{+150}_{-120}	$2.56^{+0.26}_{-0.22}$	$0.7^{+1.4}_{-0.4}$	$2.1^{+5.3}_{-1.4} \times 10^{-1}$
graphite	2004-08-16	-3811	$2.79^{+0.08}_{-0.05}$	5840^{+780}_{-600}	$0.3^{+0.3}_{-0.2}$	$14.44^{+0.36}_{-0.34}$	760^{+270}_{-210}	$2.44^{+0.36}_{-0.34}$	$2.5^{+3.1}_{-1.6}$	$2.7^{+12.9}_{-2.2} \times 10^{-6}$
graphite	2015-03-06	43	$5.48^{+0.01}_{-0.01}$	3410^{+190}_{-130}	$0.2^{+0.3}_{-0.2}$	$14.53^{+0.13}_{-0.08}$	1820^{+120}_{-190}	$3.19^{+0.13}_{-0.08}$	$13.1^{+3.5}_{-2.3}$	$3.9^{+5.8}_{-2.8} \times 10^{-6}$
graphite	2015-05-29	127	$4.5^{+0.02}_{-0.01}$	5600^{+3810}_{-2110}	$5.6^{+1.7}_{-2.4}$	$14.69^{+0.16}_{-0.13}$	1300^{+140}_{-110}	$2.92^{+0.16}_{-0.13}$	$20.9^{+3.2}_{-2.0}$	$1.6^{+0.5}_{-0.4} \times 10^{-4}$
graphite	2015-08-03	193	$4.36^{+0.03}_{-0.02}$	6970^{+3930}_{-2520}	$5.5^{+2.1}_{-2.8}$	$14.75^{+0.18}_{-0.14}$	1220^{+100}_{-90}	$2.81^{+0.18}_{-0.14}$	$21.8^{+3.1}_{-1.9}$	$2.0^{+0.7}_{-0.5} \times 10^{-4}$
graphite	2015-09-28	249	$4.25^{+0.04}_{-0.02}$	7900^{+5070}_{-3320}	$5.7^{+2.8}_{-3.6}$	$14.72^{+0.22}_{-0.16}$	1200^{+110}_{-100}	$2.68^{+0.22}_{-0.16}$	$17.4^{+2.8}_{-1.7}$	$1.8^{+0.6}_{-0.5} \times 10^{-4}$
graphite	2016-08-15	571	$3.83^{+0.09}_{-0.09}$	7320^{+1070}_{-910}	$11.3^{+1.5}_{-1.5}$	$15.24^{+0.12}_{-0.12}$	670^{+40}_{-40}	$2.84^{+0.12}_{-0.12}$	$5.2^{+3.4}_{-2.0}$	$4.2^{+3.5}_{-1.9} \times 10^{-3}$
graphite	2017-08-03	924	$3.97^{+0.15}_{-0.16}$	9580^{+5420}_{-4490}	$68.2^{+32.8}_{-8.8}$	$15.0^{+0.35}_{-0.44}$	890^{+350}_{-170}	$2.4^{+0.35}_{-0.44}$	$2.4^{+3.1}_{-1.7}$	$9.5^{+30.6}_{-7.0} \times 10^{-3}$
graphite	2018-07-21	1276	$4.1^{+0.26}_{-0.2}$	6980^{+6900}_{-3100}	$441.1^{+289.3}_{-184.6}$	$15.28^{+0.26}_{-0.22}$	680^{+130}_{-110}	$2.54^{+0.26}_{-0.22}$	$0.8^{+1.5}_{-0.5}$	$2.0^{+5.3}_{-1.3} \times 10^{-1}$

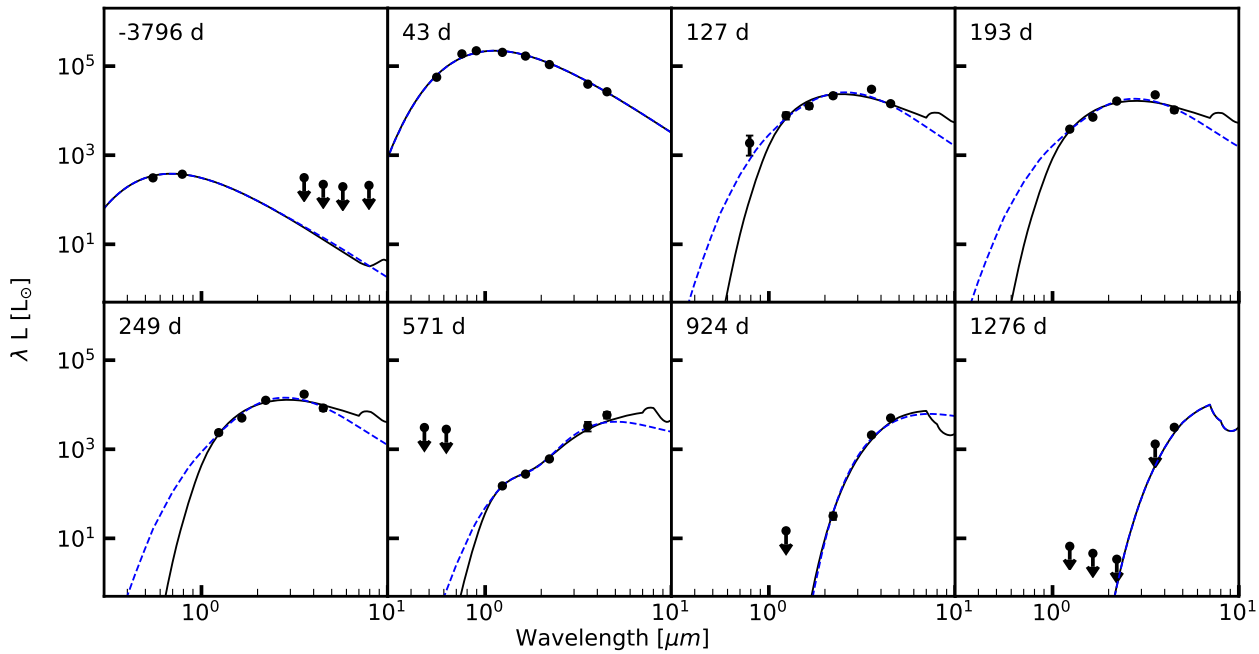

Figure 8. Evolution of the SED of M31-LRN-2015 with phases measured relative to MJD 57043.7. The SEDs in this Figure have been corrected for foreground extinction of $E(B-V) = 0.255$. The black solid line shows the best fit silicate DUSTY model and the blue dashed line the best fit graphitic model.

3.5 years show that the star possibly maintains a temperature of $\sim 10^4$ K. The lack of optical data makes this temperature mostly dependent on our prior. The dust temperature at 2.5 years appears slightly warmer than before, ∼1100 K and its internal radius shrinks to $R_{\rm in} \sim 8 \times 10^3\,{\rm R}_\odot$. However, by 3.5 years it cools again to 700 K and expands to its largest value of $R_{\rm in} \sim 3 \times 10^4\,{\rm R}_\odot$. The optical depth for these last two epochs is $\tau_V > 200$. Although our analysis for this phase is mostly based on non-detections, we suggest a possible final increase in the total luminosity of the source.

3.6 Estimate of ejecta mass

For a shell with total ejecta mass M_{ej} and radius R, the optical depth in the visual band is defined as

$$\tau_V = \frac{\kappa_V M_{\rm ej}}{4\pi R^2} \approx 3.27{\times}10^6 \left(\frac{\kappa_V}{100{\rm cm}^2/{\rm g}}\right)\left(\frac{M_{\rm ej}}{M_\odot}\right)\left(\frac{1000R_\odot}{R}\right)^2 \quad (4)$$

Provided our models fit for τ_V and the shell radius, we can estimate the total ejected mass as

$$\frac{M_{\rm ej}}{M_\odot} \approx 3.06 \times 10^{-7}\left(\frac{100{\rm cm}^2/{\rm g}}{\kappa_V}\right)\left(\frac{R}{1000R_\odot}\right)^2 \tau_V \quad (5)$$

Given that $\kappa_V \sim 50 - 100\,{\rm cm}^2/{\rm g}$ for a typical dust-to-gas ratio (Ossenkopf & Henning 1994), we derive the mass of the shell at different epochs (see Table 4). For our last epoch SED, adopting κ_V=50 we derive $M_{\rm ej} = 0.21^{0.53}_{-0.13}\,{\rm M}_\odot$, which is consistent with the values provided by Williams et al. (2015) and MacLeod et al. (2017).

4 DISCUSSION

4.1 The origin of the precursor emission

Our observations show an increase in the luminosity prior to the primary transient. One possible origin for the brightening is the formation of an optically thick photosphere, caused by an isothermal mass outflow from the system. For the outflow to become optically thick, the mass loss rate must be sufficiently high to produce a photosphere at radius $R_{\rm out} \geqslant a$, where a is the binary separation.

In order to infer the mass loss required to power this emission, we first reconstruct the total luminosity of the system (see Figure 10). We assume a black body emission at the estimated temperature of the progenitor star ($T_{\rm out} = 4300$ K). Scaling the synthetic photometry of the black body to the observed flux in r-band allows us to estimate the total bolometric luminosity of the system. We examine the effect of varying $T_{\rm out}$ between 3500 and 8000 K.

Following Pejcha (2014), the outflow luminosity is

$$L_{\rm out} = 4\pi\sigma R^2_{\tau=1} T^4_{\rm out}, \quad (6)$$

where $R_{\tau=1}$ is the photosphere and $T_{\rm out}$ is its temperature.

$$R_{\tau=1}(t) \sim \frac{\kappa \dot{M_{\rm out}}(t)}{4\pi v_{esc}} \quad (7)$$

The time-dependent radius is characterized by the outflow's density, which is defined by the rate of mass loss and the escape velocity from the system.

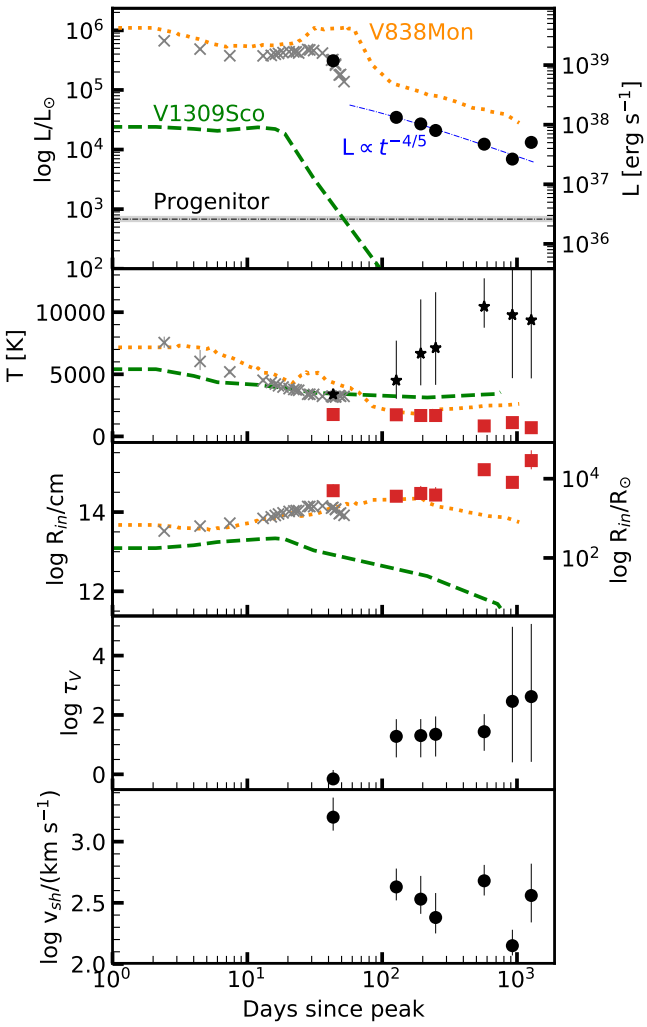

Figure 9. The top three panels show the bolometric luminosity of the system (black circles), the temperature and radius for our late time analysis of the remnant star (black stars) and the dust shell (red squares) assuming silicate dust composition. The blue line shows the expected gravitational contraction at fixed temperature (Eqn. 11). The progenitor luminosity is marked with a dashed line. For context, we also include the evolution of the transient parameters derived from the optical and NIR SEDs by MacLeod et al. (2017) (gray crosses). The coloured lines show the evolution for two Galactic stellar mergers (V838 Mon,V1309 Sco; Tylenda 2005; Tylenda et al. 2011), where we match the transients at the time of the first peak. The bottom two panels show the optical depth and the shell expansion velocity.

For the opacity of the isothermal outflow we adopt a fiducial value of $\kappa = 10^{-2}\,{\rm cm}^2\,{\rm g}^{-1}$ corresponding to electron scattering, and set the escape velocity to $v_{esc} = 250\,{\rm km\,s}^{-1}$, in agreement with previous studies of M31-LRN-2015. We set the outflow temperature to be the same as the stellar temperature of the progenitor. The resulting mass loss rate is shown in the left axis in Figure 10. Due to the lack of measurements in the IR during the precursor phase, these may be lower limits, as we ignore any contribution from longer

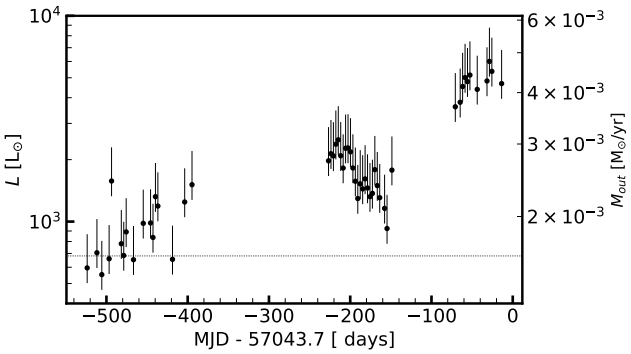

Figure 10. Bolometric luminosity of the precursor emission and mass loss rate corresponding to an isothermal outflow. The line shows the luminosity of the progenitor.

wavelengths. In addition, the value used for the opacity is also very sensitive to temperature. For example, the initiation of dust formation in the low density regions of the stream ($\rho \sim 10^{-15}\,\mathrm{cm^2\ g^{-1}}$) can lead to an increase of κ to $1\,\mathrm{cm^2\ g^{-1}}$ or even more. Alternatively, for denser regions ($\rho > 10^{-10}\,\mathrm{cm^2\ g^{-1}}$), an increase of temperature in the outflow due to shocks can increase the opacity even further to $\sim 10\,\mathrm{cm^2\ g^{-1}}$ (Ferguson et al. 2005). As a consequence, the estimated mass loss rate using an isothermal outflow assumption can underestimate the real value by a factor of $10^2 - 10^3$.

Provided that an outflow was observed up to two years before the onset of the common envelope, we argue that RLOF is a more likely scenario to explain this brightening than the Darwin instability (MacLeod et al. 2017). In this case case, the system would not have lost a significant amount of mass before the final plunge of the secondary.

4.2 Late time evolution of the remnant

The luminosity evolution of M31-LRN-2015 at late times (after the termination of the plateau) can be modelled as gravitational contraction of an inflated envelope surrounding the remnant. Similar explanations have been given for the post-outburst luminosity declines observed in V4332Sgr and V838 Mon. Tylenda et al. (2005) models the photometric evolution assuming gravitational contraction of an envelope with binding energy

$$E_\mathrm{g} = -\frac{GM_* M_\mathrm{e}}{(R_* R)^{1/2}} \tag{8}$$

where M_* is the mass of the remnant, M_e is the mass of the envelope, R_* is the inner radius of the envelope and R is the outer radius of the envelope. If the luminosity is primarily from gravitational contraction, then

$$L = -\frac{dE_\mathrm{g}}{dt} = \frac{GM_* M_\mathrm{e}}{2R_*^{1/2}} \frac{1}{R^{3/2}} \frac{dR}{dt} \tag{9}$$

and since $L = 4\pi R^2 \sigma T_\mathrm{eff}^4$,

$$\frac{dR}{R^{7/2}} = -\frac{8\pi R_*^{1/2} \sigma T_\mathrm{eff}^4}{GM_* M_\mathrm{e}} dt \tag{10}$$

Assuming constant T_eff, which is consistent with the uncertainties in our SED models, the equation can be integrated to give

$$\frac{1}{R^{5/2}} = \frac{20\pi R_*^{1/2} \sigma T_\mathrm{eff}^4}{GM_* M_\mathrm{e}} t + \frac{1}{R_0^{5/2}} \tag{11}$$

where R_0 is the envelope radius at the start of the contraction at $(t = 0)$. In this simplified model, the late-time luminosity evolution of a gravitationally settling envelope should be $L \propto t^{-4/5}$, which is plotted in the upper panel of Figure 9. This trend, similar to the one for V838 Mon, is observed until 2.5 years after peak. After that, the object seems to increase in luminosity at later times, possibly due to shocks in the system.

4.3 The effect of dust driven winds

Dust-driven winds are one of the main mechanisms in removing the extended envelopes in asymptotic giant-branch (AGB) stars. The low-temperature and high density environments generated by stellar pulsations are suitable sites for dust growth. Because of the coupling between dust and gas, the radiation pressure from the star on dust grains provides an efficient way to accelerate the outermost layers to super-sonic velocities.

In the case of stellar mergers or successful CE remnants, the envelope has an expanding unbound component, but there is also a significant amount of gas which is still gravitationally bound to the system (Pejcha et al. 2016a; MacLeod et al. 2018). If this gas is located beyond the dust condensation radius R_C, the dust grains will be able to form and grow. The radiation pressure on the bound gas will eventually accelerate the grains to super-sonic speeds and allow gas to escape from the system.

Following Glanz & Perets (2018), we define the dust condensation radius as

$$R_C = 0.5^{2/5} \left(\frac{T_C}{T_*}\right)^{-2} R_* \tag{12}$$

Assuming the progenitor parameters (T_*, R_*) derived in Section 3.3, a condensation temperature of $T_C = 1500\,\mathrm{K}$ will be achieved at $R_C \simeq 280\,\mathrm{R_\odot}$. This radius is well within the stellar photosphere of the nova, which is located at $\sim 10^4\,\mathrm{R_\odot}$, according to the analysis shown in Figure 9.

Although a detailed analysis of the dust-driven outflows for M31-LRN-2015 is outside of the scope of this work, we would like to highlight that this process may provide the long-sought channel for unbinding large part of the gas from binary systems after the spiral-in and common-envelope ejection had taken place.

5 SUMMARY AND CONCLUSIONS

In this work we have made an extended observational study of the stellar merger M31-LRN-2015, from 5 years prior the peak, to 5 years after the peak. The main conclusions of our study are:

- The progenitor of M31-LRN-2015 did not have a detectable dust emission component, which sets an upper limit

on the dust masses between $10^{-6.4}$ and $10^{-9.7}$ $M_\odot$ for optically thin dust with temperatures of 250 K and 1500 K respectively.

- M31-LRN-2015 began to brighten 2 years before peak. At about ~ -200 days the lightcurve dimmed by 1 mag, but the brightening resumed shortly afterwards. This complex luminosity evolution is best explained by the RLOF of the primary and mass loss from L2 point, which results in an optically-thick outflow with a mass loss rate of $\dot{M}_{\rm out} > 10^{-3}\,M_\odot$.
- The lightcurve of the precursor may show a period of 16.8±0.3 days in the dimming phase and 28.1±1.4 days in the brightening phase. Although the significance of these periods detections are low, we tentatively attribute this periodicity to the characteristics of the outflow from the binary, analogous to the trend observed in V1309 Sco.
- The spectroscopic evolution of the merger initially shows a 5000 K continuum with a superposed forest of narrow absorption lines from low ionization elements. After peak, the temperature of the continuum quickly drops, and strong molecular absorption features of TiO and VO appear at +47 days. By +140 days, the object has no detectable emission blueward of 8000 Å and its spectrum resembles a Mira-like M9e type star.
- Before peak, the spectrum shows an Hα emission component centred at the rest-frame velocity. The line temporarily disappears during the plateau phase, and then reappears with a blueshift of $\sim$300 km s^{-1}. The redshifted component is likely obscured by dust formed in the eruption.
- During the lightcurve plateau, the SED implies an optically thin dust shell outside the expanding photosphere of the remnant star. For gas at the system's escape velocity, the shell would have been ejected about half a year before the nova event, coinciding with the last brightening episode in the precursor emission.
- After the end of the plateau, the luminosity decreases at a rate consistent with a gravitationally settling giant star. While the merger remnant may become hotter with time, the dust shell cools down from $\sim$1700 K to $\sim$ 700 K.
- At late times, the ejecta forms an optically thick ($\tau_V \sim 400$) shell that totally obscures the stellar remnant in optical and NIR wavelengths. The shell has an estimated mass of $M_{\rm ej} \sim 0.2\,M_\odot$, in agreement with previous works. Its inner radius is located beyond the dust condensation radius, allowing radiation pressure to further accelerate this dusty matter.

The data and analysis presented in this work shows the importance of late time follow-up for a stellar merger in the infrared, revealing the fast dust formation mechanisms, which quickly obscure the nova remnant. Due to its large optical depth, the late-time merger remnant is undetectable in optical and near-infrared wavelenghts, although still visible in the mid-infrared. Some of the SPRITEs (eSPecially Red Intermediate-luminosity Transient Events) reported by the SPIRITS survey (Kasliwal et al. 2017; Jencson et al. 2019b) show similar characteristics to M31-LRN-2015 at late times, and may also be stellar mergers. The progressive evolution of the object's emission into longer wavelengths makes it an exciting target for the James Webb Space Telescope (JWST).

ACKNOWLEDGEMENTS

N. B. would like to thank O. Pejcha and M. MacLeod for useful discussions, A. Kurtenkov and S. C. Williams for making available the spectra of M31-LRN-2015, A. Pastorello for data on AT2017fjs, and T. Kaminski for the spectrum of V1309Sco. To M. Fraser, D. Perley, and R. M. Wagner for observations and data reduction, and to T. Szalai for the dust emission models. This work is part of the research programme VENI, with project number 016.192.277, which is (partly) financed by the Netherlands Organisation for Scientific Research (NWO). SK acknowledges the financial support of the Polish National Science Center (NCN) through the OPUS grant 2018/31/B/ST9/00334. P.E.N. acknowledges support from the DOE under grant DE-AC02-05CH11231, Analytical Modeling for Extreme-Scale Computing Environments. CSK is supported by NSF grants AST-1908570 and AST-1814440. The Intermediate Palomar Transient Factory project is a scientific collaboration among the California Institute of Technology, Los Alamos National Laboratory, the University of Wisconsin, Milwaukee, the Oskar Klein Center, the Weizmann Institute of Science, the TANGO Program of the University System of Taiwan, and the Kavli Institute for the Physics and Mathematics of the Universe. The WHT spectrum was taken under program (2014B/P29). This research used resources of the National Energy Research Scientific Computing Center, a DOE Office of Science User Facility supported by the Office of Science of the U.S. Department of Energy under Contract No. DE-AC02-05CH11231.

Some of the data presented herein were obtained at the W.M. Keck Observatory, which is operated as a scientific partnership among the California Institute of Technology, the University of California and the National Aeronautics and Space Administration. The Observatory was made possible by the generous financial support of the W.M. Keck Foundation. The authors wish to recognize and acknowledge the very significant cultural role and reverence that the summit of Maunakea has always had within the indigenous Hawaiian community. We are most fortunate to have the opportunity to conduct observations from this mountain. This work is based in part on observations made with the Large Binocular Telescope. The LBT is an international collaboration among institutions in the United States, Italy and Germany. The LBT Corporation partners are: The University of Arizona on behalf of the Arizona university system; Istituto Nazionale di Astrofisica, Italy; LBT Beteiligungsge- sellschaft, Germany, representing the Max Planck Society, the Astrophysical Institute Potsdam, and Heidelberg University; The Ohio State University; The Research Corporation, on behalf of The University of Notre Dame, University of Minnesota and University of Virginia. Part of this research was carried out at the Jet Propulsion Laboratory, California Institute of Technology, under a contract with the National Aeronautics and Space Administration. We acknowledge Telescope Access Program (TAP) funded by the NAOC, CAS, and the Special Fund for Astronomy from the Ministry of Finance. This work is based in part on observations made with the Spitzer Space Telescope, which is operated by the Jet Propulsion Laboratory, California Institute of Technology under a contract with NASA. This research made use of Astropy,[4] a community-developed core Python package for Astronomy (Astropy Collaboration et al. 2013, 2018).

[4] http://www.astropy.org

REFERENCES

Adams S. M., Kochanek C. S., 2015, MNRAS, 452, 2195
Adams S., Kochanek C. S., Dong S., Wagner R. M., 2015a, The Astronomer's Telegram, 7468
Adams S., Kochanek C. S., Dong S., Wagner R. M., 2015b, The Astronomer's Telegram, 7485, 1
Adams S. M., Kochanek C. S., Prieto J. L., Dai X., Shappee B. J., Stanek K. Z., 2016, MNRAS, 460, 1645
Adams S. M., Kochanek C. S., Gerke J. R., Stanek K. Z., Dai X., 2017, MNRAS, 468, 4968
Adams S. M., et al., 2018, PASP, 130, 034202
Astropy Collaboration et al., 2013, A&A, 558, A33
Astropy Collaboration et al., 2018, AJ, 156, 123
Bersier D., Kochanek C. S., Wagner R. M., Adams S., Dong S., 2015, The Astronomer's Telegram, 7537
Blagorodnova N., et al., 2017, ApJ, 834, 107
Bond H. E., Bedin L. R., Bonanos A. Z., Humphreys R. M., Monard L. A. G. B., Prieto J. L., Walter F. M., 2009, ApJ, 695, L154
Botticella M. T., et al., 2009a, MNRAS, 398, 1041
Botticella M. T., et al., 2009b, MNRAS, 398, 1041
Castelli F., Kurucz R. L., 2004, astro-ph/0405087,
Chambers K. C., et al., 2016, arXiv:1612.05560,
Chemin L., Carignan C., Foster T., 2009, ApJ, 705, 1395
Darwin G. H., 1879, Proceedings of the Royal Society of London Series I, 29, 168
Dong S., Kochanek C. S., Adams S., Prieto J.-L., 2015, The Astronomer's Telegram, 7173
Draine B. T., Lee H. M., 1984, ApJ, 285, 89
Draine B. T., et al., 2014, ApJ, 780, 172
Elitzur M., Ivezić Ž., 2001, MNRAS, 327, 403
Fabrika S., et al., 2015, The Astronomer's Telegram, 6985, 1
Fazio G. G., et al., 2004, The Astrophysical Journal Supplement Series, 154, 10
Ferguson J. W., Alexander D. R., Allard F., Barman T., Bodnarik J. G., Hauschildt P. H., Heffner-Wong A., Tamanai A., 2005, ApJ, 623, 585
Freedman W. L., Madore B. F., 1990, ApJ, 365, 186
Gehrz R. D., et al., 2007, Review of Scientific Instruments, 78, 011302
Geier S., Pessev P., 2015, The Astronomer's Telegram, 8220, 1
Giallongo E., et al., 2008, A&A, 482, 349
Glanz H., Perets H. B., 2018, MNRAS, 478, L12
Gunn J. E., Stryker L. L., 1983, ApJS, 52, 121
Harmanen J., McCollum B., Laine S., Rottler L., Bruhweiler F. C., 2015, The Astronomer's Telegram, 7595, 1
Hill J. M., Green R. F., Slagle J. H., 2006, in Society of Photo-Optical Instrumentation Engineers (SPIE) Conference Series. p. 62670Y, doi:10.1117/12.669832
Hodgkin S. T., et al., 2015, The Astronomer's Telegram, 6952, 1
Ivanova N., et al., 2013a, A&A Rev., 21, 59
Ivanova N., Justham S., Avendano Nandez J. L., Lombardi J. C., 2013b, Science, 339, 433
Ivezic Z., Elitzur M., 1997, MNRAS, 287, 799
Ivezic Z., Nenkova M., Elitzur M., 1999, astro-ph/9910475,
Izzard R. G., Hall P. D., Tauris T. M., Tout C. A., 2012, in IAU Symposium. pp 95–102, doi:10.1017/S1743921312010769
Jacoby G. H., Hunter D. A., Christian C. A., 1984, ApJS, 56, 257
Jencson J. E., et al., 2019a, ApJ, 880, L20
Jencson J. E., et al., 2019b, ApJ, 886, 40
Kamiński T., Tylenda R., 2011, A&A, 527, A75
Kamiński T., Mason E., Tylenda R., Schmidt M. R., 2015, A&A, 580, A34
Kamiński T., et al., 2017, A&A, 599, A59
Kasliwal M. M., 2012, PASA, 29, 482
Kasliwal M. M., et al., 2017, ApJ, 839, 88
Keenan P. C., Garrison R. F., Deutsch A. J., 1974, ApJS, 28, 271
Kochanek C. S., Adams S. M., Belczynski K., 2014, MNRAS, 443, 1319
Kulkarni S. R., 2013, The Astronomer's Telegram, 4807
Kurtenkov A. A., et al., 2015a, A&A, 578, L10
Kurtenkov A., Ovcharov E., Nedialkov P., Kostov A., Bachev R., Dimitrova R. V. M., Popov V., Valcheva A., 2015b, The Astronomer's Telegram, 6941, 1
Kurtenkov A., et al., 2015c, The Astronomer's Telegram, 7150
Laor A., Draine B. T., 1993, ApJ, 402, 441
Law N. M., et al., 2009, PASP, 121, 1395
Law N. M., et al., 2010, in Ground-based and Airborne Instrumentation for Astronomy III. p. 77353M, doi:10.1117/12.857400
Lipunov V. M., et al., 2017, arXiv:1704.08178,
Lodders K., 2003, ApJ, 591, 1220
Lomb N. R., 1976, Ap&SS, 39, 447
MacLeod M., Macias P., Ramirez-Ruiz E., Grindlay J., Batta A., Montes G., 2017, ApJ, 835, 282
MacLeod M., Ostriker E. C., Stone J. M., 2018, ApJ, 868, 136
Masci F. J., et al., 2017, PASP, 129, 014002
Mason E., Diaz M., Williams R. E., Preston G., Bensby T., 2010, A&A, 516, A108
Mathis J. S., Rumpl W., Nordsieck K. H., 1977, ApJ, 217, 425
Metzger B. D., Pejcha O., 2017, MNRAS, 471, 3200
Montalto M., Seitz S., Riffeser A., Hopp U., Lee C.-H., Schönrich R., 2009, A&A, 507, 283
Mould J., et al., 1990, ApJ, 353, L35
Munari U., et al., 2002, A&A, 389, L51
Oke J. B., et al., 1995, PASP, 107, 375
Ossenkopf V., Henning T., 1994, A&A, 291, 943
Ovcharov E., Kurtenkov A., Valcheva A., Nedialkov P., 2015, The Astronomer's Telegram, 6924, 1
Paczynski B., 1976, in Eggleton P., Mitton S., Whelan J., eds, IAU Symposium Vol. 73, Structure and Evolution of Close Binary Systems. p. 75
Pastorello A., Fraser M., 2019, Nature Astronomy, 3, 676
Pastorello A., et al., 2019a, A&A, 625, L8
Pastorello A., et al., 2019b, A&A, 630, A75
Pejcha O., 2014, ApJ, 788, 22
Pejcha O., Metzger B. D., Tomida K., 2016a, MNRAS, 455, 4351
Pejcha O., Metzger B. D., Tomida K., 2016b, MNRAS, 461, 2527
Pejcha O., Metzger B. D., Tyles J. G., Tomida K., 2017, ApJ, 850, 59
Pessev P., Geier S., Kurtenkov A., Nielsen L. D., Tomov T., 2015a, The Astronomer's Telegram, 7272, 1
Pessev P., Geier S., Kurtenkov A., Nielsen L. D., Slumstrup D., Tomov T., 2015b, The Astronomer's Telegram, 7572, 1
Pessev P., Geier S., Stritzinger M., Kurtenkov A., Tomov T., 2015c, The Astronomer's Telegram, 7624, 1
Pessev P., Geier S., Stritzinger M., Kurtenkov A., Tomov T., 2015d, The Astronomer's Telegram, 8059, 1
Prieto J. L., Sellgren K., Thompson T. A., Kochanek C. S., 2009, ApJ, 705, 1425
Rahmer G., Smith R., Velur V., Hale D., Law N., Bui K., Petrie H., Dekany R., 2008, in Ground-based and Airborne Instrumentation for Astronomy II. p. 70144Y, doi:10.1117/12.788086
Rasio F. A., 1995, ApJ, 444, L41
Rau A., et al., 2009, PASP, 121, 1334
Rich R. M., Mould J., Picard A., Frogel J. A., Davies R., 1989, ApJ, 341, L51
Scargle J. D., 1982, ApJ, 263, 835
Schlafly E. F., et al., 2012, ApJ, 756, 158
Schlegel D. J., Finkbeiner D. P., Davis M., 1998, ApJ, 500, 525
Seifert W., et al., 2003, in Iye M., Moorwood A. F. M., eds, Proc. SPIEVol. 4841, Instrument Design and Performance for Optical/Infrared Ground-based Telescopes. pp 962–973, doi:10.1117/12.459494

Shumkov V., et al., 2015a, The Astronomer's Telegram, 6911
Shumkov V., et al., 2015b, The Astronomer's Telegram, 6951, 1
Smith N., et al., 2016, MNRAS, 458, 950
Srivastava M., Ashok N. M., Banerjee D. P. K., Venkataraman V., 2015, The Astronomer's Telegram, 7236, 1
Steele I. A., Williams S. C., Darnley M. J., Bode M. F., Barnsley R. M., Smith R. J., Jermak H. E., 2015, The Astronomer's Telegram, 7555, 1
Tylenda R., 2005, A&A, 436, 1009
Tylenda R., Kamiński T., 2016, A&A, 592, A134
Tylenda R., Crause L. A., Górny S. K., Schmidt M. R., 2005, A&A, 439, 651
Tylenda R., et al., 2011, A&A, 528, A114
Wagner R. M., Starrfield S. G., Wilber A., Kochanek C. S., Dong S., Prieto J.-L., Adams S., 2015, The Astronomer's Telegram, 7208
Werner M. W., et al., 2004, The Astrophysical Journal Supplement Series, 154, 1
Williams S. C., Darnley M. J., Bode M. F., Steele I. A., 2015, ApJ, 805, L18
Wizinowich P. L., et al., 2006, PASP, 118, 297
Wozniak P. R., 2000, Acta Astron., 50, 421
Yaron O., Gal-Yam A., 2012, PASP, 124, 668

This paper has been typeset from a TEX/LATEX file prepared by the author.